Formation and elimination of anti-site defects during crystallization in perovskite $Ba_{1-x}Sr_xLiF_3$

A. Düvel[1,2,*], L. M. Morgan[1], C. Vinod Chandran[2], P. Heitjans[2], D.C. Sayle[1,*]

[1] School of Physical Sciences, University of Kent, Canterbury, Kent CT2 7NH, UK
[2] Institute of Physical Chemistry and Electrochemistry, Leibniz Universität Hannover, Callinstr. 3-3a, D-30167 Hannover, Germany

Abstract

The defect density of a material is decisive for its physical, chemical and mechanical properties. Accordingly, defect tuning is desirable for applications spanning, e.g., batteries, fuel cells, electronics, optics, catalysis and mechanical strength and resilience. Here we simulate the mechanochemical synthesis of the perovskite $Ba_{1-x}Sr_xLiF_3$ by compressing a $BaLiF_3$ nanoparticle with a $SrLiF_3$ nanoparticle under conditions likely to occur during high-energy ball milling. We investigate the crystallization process and the ionic mobility of the system and compare with experiment. Animations of the crystallization, simulated under high pressure, revealed that cations, within the crystallization front, would commonly condense onto 'incorrect' lattice sites, in some cases eventually leading to the formation of anti-site defects. However, most of these cations would then re-amorphise and the 'correct' cation would take its place – rectifying the defect. Crucially, it is the amorphous/crystalline interface that enables such repair because the ions are mobile in this region. The simulations reveal high ion mobility close to the anti-site defects and other defective regions, but no ion mobility in the defect free regions of $BaLiF_3$. The MD simulations indicate that high-energy ball milling might reduce the anti-site defect density in a material by exposing these defects to the surface or creating amorphous regions within the crystallite which then would allow localized recrystallization, enabling defect repair. This assumption is a possible explanation for the reduced ion mobility, revealed by NMR spectroscopy, and, thus, most likely smaller defect density in $BaLiF_3$ prepared by high-energy ball milling compared to thermally synthesized $BaLiF_3$ samples.

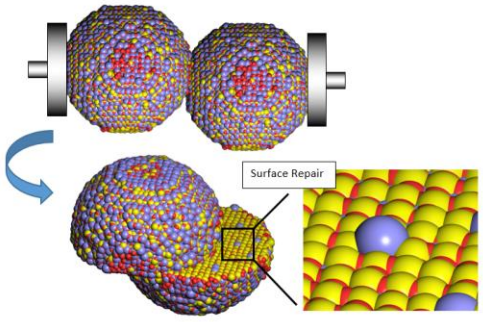

Introduction

The properties of a functional material are governed by its defect density; the latter derives, apart from temperature and size of the system, from the synthetic pathway used in its fabrication. Typically, high defect densities, and associated high ionic mobility, are desirable in ceramics with applications for fuel cells or batteries[1,2], albeit defects can sometimes reduce the ionic conductivity[3,4]. Conversely, materials with low defect densities are inter alia needed for LEDs[5,6], photovoltaics[7] and optical devices[8,9]. Moreover, defect tuning is widely used to modulate the catalytic activity of a material[10,11]. Defect tuning is therefore pivotal to the exploitation of a functional material possessing a diverse range of properties and hence applications. Defect control, via 'work hardening' - analogous to ball milling - strengthens a material via plastic deformation and recrystallization below its melting temperature and has been exploited for millennia. However, the implications of defect modulation of nanomaterials are less well developed. Such knowledge will be critical for the mechanical resilience and preservation of properties of the functional material during its operational lifespan. [12].

An important class of materials, with applications including catalyst[13], ion conductor[14-16], dielectric[17,18], piezoelectric[19], photovoltaic[7,20], are the perovskites, ABX_3. In this class, $BaLiF_3$ is a rare example of a cation inverted perovskite[21]. It is a potential material for vacuum-ultraviolet lasers[22,23] and lenses[8] because of its large band-gap. The material is also an interesting model system to study ion conduction, since it contains two light ions, F^- and Li^+, which are likely to be mobile in the system. Although this issue was addressed in theoretical studies[24,25], there is a lack of experimental data. Previously, we reported a higher ionic conductivity of nanocrystalline $BaLiF_3$ prepared by ball milling equimolar mixtures of BaF_2 and LiF, compared to thermally prepared micro or single crystalline $BaLiF_3$.[26] Interestingly the higher ionic conductivity comes along with a smaller ionic mobility of the majority of the ions, as revealed by temperature variable ^{7}Li NMR measurements.[27]

Mechanosynthesis generally offers a fast, easy and inexpensive method of fabricating nanocrystalline materials[28,29] including metastable ceramics which are difficult to prepare using alternative methods[30-33]. Hence, it was possible to substitute up to 40 % of the Ba ions in $BaLiF_3$ by Sr ions using a mechanochemical approach, forming metastable $Ba_{1-x}Sr_xLiF_3$, which exhibits a very similar ionic conductivity as mechanochemically prepared $BaLiF_3$[30]. The reaction mechanism was investigated by ^{19}F magic angle spinning (MAS) NMR spectroscopy. It was found that the replacement of Ba ions by Sr ions starts after the formation of $BaLiF_3$[30].

In this study, we use Molecular Dynamics (MD) to simulate a part of the ball milling process, i.e. the impact of a milling ball compressing a $BaLiF_3$ nanoparticle with a $SrLiF_3$ nanoparticle leading to the formation of $Ba_{1-x}Sr_xLiF_3$.

Specifically, we simulate the crushing and subsequent amorphisation of $BaLiF_3$/$SrLiF_3$ nanoparticles under high temperature and pressure[34], the amorphous-to-crystalline phase change, and finally, the F and Li ionic mobility within the 'ball milled' model system. We couple our simulations with ^{19}F and ^{7}Li NMR measurements on the real materials, synthesized using high-energy ball milling and thermal annealing, to determine the ionic mobility.

Methods

Computational

Generating Atomistic Models

A spherical nanoparticle of $BaLiF_3$ with cation inverted perovskite structure was generated, using crystallographic data taken from ref [35]. In one half of the nanoparticle, the Ba ions were replaced by Sr; the number of atoms in the simulation cell was: Ba = 4133, Sr = 4127, Li = 8186, F = 24706. We note that the stoichiometry was not set exactly to ABX_3, this was to ensure that the stoichiometry did not bias artifically the evolution of a perovskite structure. The nanoparticle was then 'crushed', using MD simulation, performed at high pressure and temperature, to mirror an impact of a milling ball onto the particle, fig 1. Specifically, MD simulation was performed at 5 GPa and 1000 K for 107 ns under an NPT ensemble (constant Number of ions, constant Pressure and constant Temperature). The simulation thus facilitates a $BaLiF_3$ nanoparticle crushed together with a $SrLiF_3$ nanoparticle. Under these simulations conditions of crushing a $BaLiF_3$ nanoparticle with a $SrLiF_3$ nanoparticle, the $SrLiF_3$ nanoparticle first armorphised and then crystallized, which required about 107 ns. After crystallisation, ionic mobility data of F and Li ions in the model system was collected (at 0 Pa and 600 K).

This (single) simulation required 250,000 cpu hours; the high computational cost was attributed to crystallization 'errors' and repair mechanisms. Viewing the crystallization animations revealed that several defects evolved in each atomic layer – most of which were repaired. We presume that this 'defect evolution and repair' process resulted in the high computation cost. We *surmise* that the crystallization front only moved forward once most of the defects were repaired enabling a lower configurational energy. It is likely that the Madelung field is integral to crystallization and that any perturbation of this field reduces the propensity for other ions to

spontaneously order at the crystallization front. Previous simulations, performed on binary oxides, such as CeO_2 and TiO_2[36,37], typically required an order of magnitude less computational time.

Potential Model

The Born model of the ionic solid was used to describe the $Ba_{1-x}Sr_xLiF_3$ in which the component ions interact via short-range parameterized interactions coupled with long-range Coulombic interactions, equation (1).

$$E(r_{ij}) = \sum_{ij} \frac{Q_i Q_j}{4\pi\varepsilon_o r_{ij}} + \sum_{ij} A \exp\left(\frac{-r_{ij}}{r}\right) - C r_{ij}^{-6} \quad (1)$$

The potential parameters, table 1 (SI), were taken from ref. [24] using a rigid ion model. The Sr-F interaction was derived by potential fitting to the SrF_2 structure and elastic[38] and dielectric[39] properties using the GULP code[40]. All the MD simulations were performed using the DL_POLY code[41].

We note that the potential model was capable of generating a perovskite-structured $Ba_{1-x}Sr_xLiF_3$ nanomaterial together with defects typically found in the real material such as anti-site defects and stacking faults. Moreover, such crystal and micro structures evolved from an amorphous precursor, where interatomic distances were far from equilibrium values. This proffers confidence in that the potential model is both robust and accurate.

Experimental

Synthesis

$Ba_{1-x}Sr_xLiF_3$ was prepared by milling mixtures of LiF (99.99%, Alfa Aesar), BaF_2 (99.99%, Sigma Aldrich) and SrF_2 (99.99%, Alfa Aesar) in a planetary ball mill (Pulverisette 7 *premium line*, Fritsch, Germany) with an overall mass of 2.000(1) g employing a milling beaker (45 mL) filled with 140 milling balls with a diameter of 5 mm made of stabilized ZrO_2 (Fritsch, Germany). The total milling times were altered for the different compositions. If not stated otherwise, for the pure $BaLiF_3$, an equimolar mixture of BaF_2 and LiF was milled for 6 h. The $Ba_{1-x}Sr_xLiF_3$ samples were milled for 20 h. The microcrystalline $BaLiF_3$ is identical to the one reported in refs. [26,27] prepared by annealing mechanosynthesised $BaLiF_3$, which was since then stored under vacuum in a glass ampoule and stayed phase pure this way.

The $BaLiF_3$ single crystal is identical to the one reported in ref. [26] and was prepared by the procedure described there: At first, the starting materials, BaF_2 (crystal pieces) and LiF (GFI, 'optical grade') were purified by a pre-treatment, i.e. the materials were treated with hydrofluoric acid at elevated temperatures. Subsequently, they were mixed in the required ratio and subjected to a zone melting procedure under HF. Since $BaLiF_3$ melts incongruently at about 1100 K, the composition of the starting materials has to deviate from the composition of the crystal. The chosen composition was $Ba_{0.86}Li_{1.14}F_{2.86}$. The crystal was grown in a platinum crucible by conventional Czochralski technique with radio frequency (RF)-heating and automatic diameter control. In order to suppress oxidation of the melt, the crystal was grown in an atmosphere consisting of Ar and CF_4. The growth rate was 2 mm/h and the rotation varied from 10 to 25 min^{-1}. The obtained colorless crystal was 70 mm in length and 18 mm in diameter. XRPD confirmed phase purity[26].

Measurements

The ^7Li and ^{19}F NMR measurements were conducted with two different NMR spectrometers. The high temperature decoupling experiments were done with a laser heated MAS probe (Bruker Biospin) at an Avance III spectrometer (Bruker Biospin) operating at $\nu_0(^{19}F)$ = 564.7 MHz and $\nu_0(^7Li)$ = 233.3 MHz. The spinning rate of the rotor was set to 3 kHz. Freshly evaporated nitrogen gas was used as bearing gas. For the ^{19}F NMR measurements a $\pi/2$ pulse with duration of 2.5 µs, for the ^7Li NMR measurements a $\pi/2$ pulse with duration of 3.5 µs was used. Four scans were accumulated for each spectrum with a waiting time of 6 x the spin lattice relaxation time, T_1, between the scans to record fully relaxed spectra. The decoupling experiments were done with a robust decoupling program with frequency sweep[42].

The static ^{19}F and ^{7}Li NMR experiments were done with an MSL 400 spectrometer (Bruker Biospin) connected to an Oxford cryomagnet with a nominal field of 9.4 T corresponding to $\nu_0(^{19}F)$ = 376.5 MHz and $\nu_0(^{7}Li)$ = 155.4 MHz. The ^{19}F NMR measurements were performed with a modified 7 mm MAS probe (Bruker), the ^{7}Li NMR measurements with a commercial high-temperature probe (Bruker Biospin). For all measurements the saturation recovery sequence[43] was used, followed by an adjustable waiting time (set to 6 x T_1 to record fully relaxed spectra) and a single $\pi/2$ pulse with duration of 3.4 µs (^{19}F) and 1.8 µs (^{7}Li), respectively. Measurements were done at samples sealed in glass ampoules. The samples were dried in vacuum at ca. 380 K for at least 24 h prior to sealing.

Results

Simulation

Crystallization Simulated 'ball milling' of the $BaLiF_3/SrLiF_3$ nanosystem results in the amorphisation of the $SrLiF_3$, which thus can be understood as a reaction of the $BaLiF_3$ nanoparticle with an amorphous mixture of SrF_2 and LiF similar to experimental observations[30], and leaching of Ba ions into the amorphous material, fig 1(a,b). The (Sr-rich) $Ba_{1-x}Sr_xLiF_3$ then starts to crystallize – templated by $BaLiF_3$, which acts as a nucleating seed, figs. 1 (c, d).

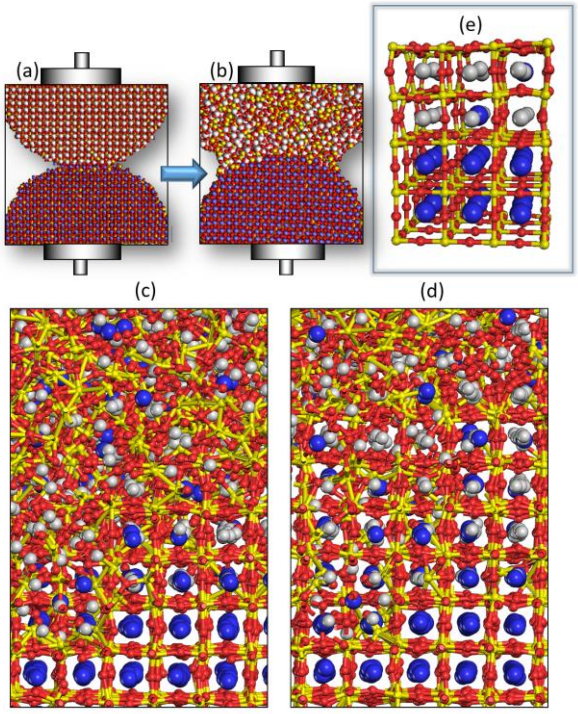

Fig. 1: MD Simulation of mechanosynthesis of $Ba_{1-x}Sr_xLiF_3$. (a) Spherical nanoparticles of $BaLiF_3$ and $SrLiF_3$, simulated using MD under 5 GPa compression at 1000 K. (b) Amorphisation of the $SrLiF_3$ nanoparticle and leaching of the Ba ions into the amorphous region. (c,d) Snapshots of a segment of the model showing the crystallization of the system after (c) 27 ns and (d) 78 ns. (e) final, low temperature, structure of a segment of the model showing the perovskite crystal structure. Ba ions are colored blue, Sr ions are white, Li ions are yellow and F ions, red.

During crystallization, Li and Ba/Sr ions, in the amorphous region, condense onto the crystalline region and compete for the two (perovskite) cation sites. Animations of the simulated crystallization (cf. SI) reveal that cations often condense onto 'incorrect' lattice sites – such as Li on A sites and Ba/Sr on B sites leading to anti-site defects. However, most of these cations re-amorphise and are then replaced by the 'correct' cation – fed from the amorphous region -, repairing the anti-site defect, see fig. 2.

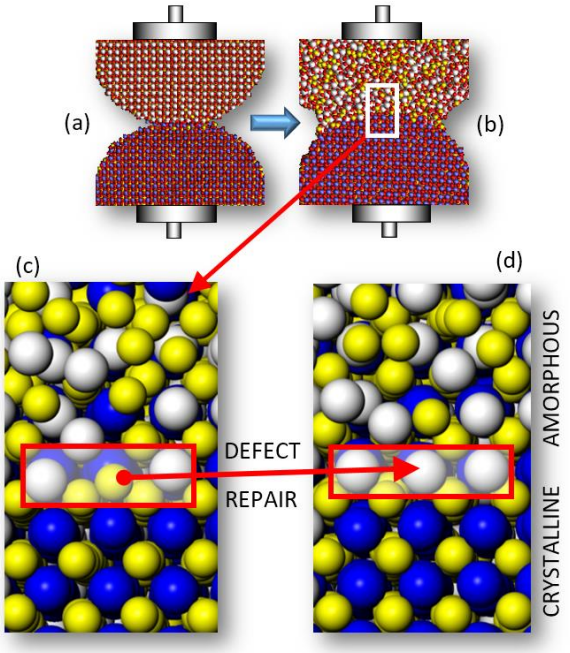

Fig. 2: Repair of substitutional defects. (a) Model nanoparticle crushed under simulated ball milling resulting in amorphisation of the $SrLiF_3$, (b). (c) Section cut through the model system during crystallization showing a Li ion, colored yellow, that has crystallized (erroneously) onto the A-site of the perovskite structure. (d) as (c) but after further MD simulation, which results in the Li moving off the A-site (dissolution) and is subsequently replaced by an Sr ion repairing the defect. Li is colored yellow, Sr is white and Ba is red (F ions are not shown).

Crucially, an exchange of cations can only take place if the defect is in direct contact with the amorphous phase because it enables ion mobility. Conversely, if the crystallization front moves forward before the incorrect ions are replaced, the cations become trapped, resulting in the formation of anti-site defects, figs. 3, S1 and S2.

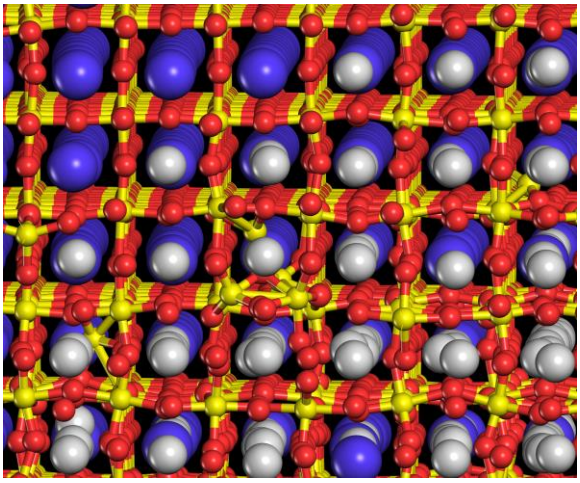

Fig. 3: A part of the crystallized system characterized by anti-site defects and Ba/Sr intermixing causing lattice distortion.

In our simulations we found the Li ions residing at A sites off center, resulting in a coordination number of 4 or 5 (seemingly depending on the number of Li ions on the site) instead of 12, see fig. S2.

It should be mentioned that the formation of Ba-Li anti-site defects has previously been postulated by several authors.[25,44-45] We therefore provide evidence that their postulate was correct and, moreover, predict a repair mechanism.

It should be noted that $SrLiF_3$, in agreement with DFT calculations[46] predicting $SrLiF_3$ to be unstable, has not yet been prepared experimentally. Following the simulation results, a synthesis at elevated pressure should be tried, because reducing the pressure towards zero in the simulation leads to a phase transformation of $SrLiF_3$ to SrF_2 and LiF, which will be discussed in detail in an upcoming paper.

Ionic mobility Analysis, using molecular graphical techniques (see supporting information for more information), reveals high F and Li ion mobility in defective regions of the $Ba_{1-x}Sr_xLiF_3$ system. These include anti-site defects, Sr/Ba intermixing and edge dislocations/stacking faults, fig 4 and SI figs S1-S2 and S6. It should be mentioned, that Zahn et al.[25] created Ba-Li anti-site defects intentionally in their simulations to get smaller activation energies for

Frenkel defect formation which are closer to experimental results.

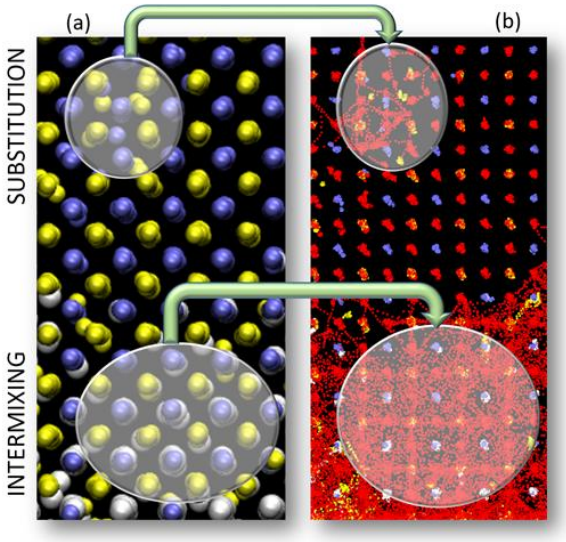

Fig. 4: F and Li ion mobility in defective regions of $Ba_{1-x}Sr_xLiF_3$ *(a) segment of the model structure showing (top) substitutional defects: Li located on perovskite A-sites and Ba located on B-sites; (bottom) intermixing of Ba and Sr ions on A-sites. (b) superimposed snapshots in time of the MD simulation showing the mobility of the F ions around the defects. We note that domains of perfect* $BaLiF_3$ *show no F or Li ion transport.*

The increased ion mobility in the areas showing Sr/Ba intermixing, which can be ascribed to geometric frustration[47], is in agreement with experiment (fig. 5), reinforcing the validity of the simulations. Conversely, domains of pristine (defect-free) $BaLiF_3$ showed no ionic mobility within the timescale of the MD simulation, figs 4 and S5.

Experiment

In fig. 5, in the two left columns, static ^{19}F NMR spectra of nanocrystalline (mechanosynthesized) and microcrystalline (annealed) $BaLiF_3$ recorded at different temperatures are shown. The static ^{19}F NMR spectrum consists of three NMR lines, which was also observed for $RbCaF_3$[48] and $RbPbF_3$[49] and is probably caused by chemical shift anisotropy (the ^{19}F MAS NMR spectrum, recorded with ν_{rot} = 60 kHz, displays a single NMR line at 66 ppm for all $BaLiF_3$ samples prepared[26]). The spectra exhibit only subtle changes with temperature. The ones of the mechanosynthesized sample show a growing bulge of the main NMR line, while the NMR spectra of the microcrystalline sample reveal an incipient coalescence of the most intense and the NMR line located at around 45 kHz, both indicating the beginning of fast motion of ions (see figs. S7a-d for ^{19}F and ^{7}Li NMR spectra of the two $BaLiF_3$ samples at higher temperature). On the right side of fig. 5, the static ^{19}F and ^{7}Li NMR spectra of $Ba_{0.74}Sr_{0.26}LiF_3$ are shown (see fig. S8 for the respective ^{7}Li NMR spectra of $BaLiF_3$). The ^{19}F NMR spectra show the emergence of a narrow NMR line at temperatures above 373 K indicating fast ion motion of the fluoride ions. Also the ^{7}Li NMR spectra show a pronounced motional narrowing which was not observed for the mechanosynthesized, pure $BaLiF_3$, see fig. S8. Hence, the replacement of a part of the Ba ions by Sr ions increases the ionic mobility, in agreement with simulation.

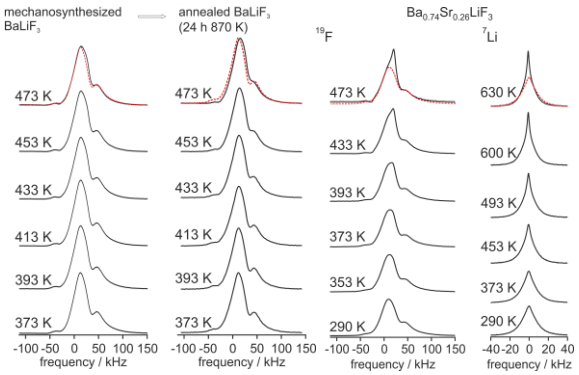

Fig. 5: Left two columns: comparison of ^{19}F *NMR spectra recorded at the temperatures indicated of mechanosynthesised (3 h 600 rpm,* ZrO_2 *milling vial set) and the annealed* $BaLiF_3$ *(24 h 870 K). Right two columns:* ^{19}F *and* ^{7}Li *NMR spectra of mechanosynthesised* $Ba_{0.74}Sr_{0.26}LiF_3$ *recorded at the temperatures indicated. (*$\nu_0(^{19}F)$ *= 376.5 MHz,* $\nu_0(^{7}Li)$ *= 155.4 MHz). For comparison the* ^{7}Li *NMR spectra recorded at 630 K and 290 K (red dashed line) as well as the* ^{19}F *NMR spectra recorded at 473 K and 373 K are superimposed.*

Since the motional narrowing of the ^{7}Li NMR spectra can be caused by both, the fast motion of the Li ions as well as the fast motion of the F ions coordinating

the Li ions due to nuclear dipole coupling, a decoupling of ^{7}Li and ^{19}F was done which suppresses the interaction between these two nuclei. This way a motional narrowing of the ^{7}Li NMR line can only be caused by a motional averaging of the Li-Li (and Li-Ba) interactions, and a motional narrowing of the ^{19}F NMR line is solely caused by a motional averaging the F-F (and F-Ba) interactions. However, it should be noted, that the F-F interaction is much stronger than the F-Li interaction, such that a pronounced motional narrowing of a ^{19}F NMR line would clearly be caused by F motion. In fig. 6 the ^{7}Li and ^{19}F NMR spectra, with the respective other nucleus decoupled, are shown for the microcrystalline and nanocrystalline $BaLiF_3$, prepared by high-energy ball milling. In agreement with ref. [27] the microcrystalline sample shows a pronounced motional narrowing of the ^{7}Li NMR line while the mechanosynthesized sample is characterized by only a slight motional narrowing. The ^{19}F NMR spectrum of the microcrystalline sample shows the emergence of a narrow line resulting from the coalescence of the NMR lines located around 30 kHz and 100 kHz, starting at ca. 610 K (see figs. S7a-d for other temperatures), while the nanocrystalline $BaLiF_3$ only shows the beginning of such a process at 740 K.

As displayed in fig. 6, both, the ^{7}Li NMR spectra and the ^{19}F NMR spectra show motional narrowing and coalescence, respectively, indicating that both ion species are mobile in both $BaLiF_3$ samples, which is in agreement with simulation. In case of the microcrystalline sample almost all Li ions appear to be mobile above 700 K, while only a fraction of the F ions are highly mobile. This seems to be in disagreement with the simulations. However, it should be noted, that for Li, much smaller jump rates (ca. 4 kHz) are sufficient for motional narrowing because of the narrow rigid lattice line widths. Conversely, F ion jump rates need to be about ten times larger than Li ion jump rates to cause motional narrowing. Computationally, the ion mobility was captured over a time span of 1 ns at 1000 K (because of computational cost). This translates to jump rates larger than 1 GHz. Accordingly, slow jumps of the Li ions would not be visible in the window of time accessible to the MD simulation. Albeit we do observe some fast Li jumps close to defects.

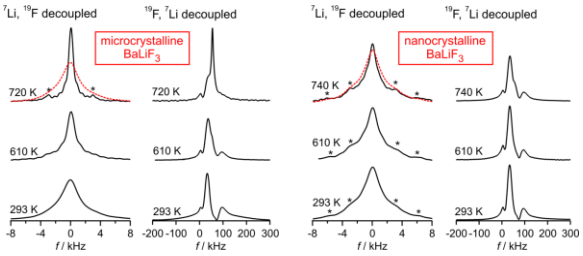

Fig 6: Left two columns: On the left ^{7}Li MAS NMR spectra with ^{19}F decoupled, on the right ^{19}F MAS NMR spectra with ^{7}Li decoupled for microcrystalline $BaLiF_3$ ($\nu_0(^{19}F)$ = 565 MHz, $\nu_0(^{7}Li)$ = 233 MHz). Right two columns: the same kind of spectra is shown for mechanosynthesized $BaLiF_3$. The spinning rate was set to 3 kHz. Asterisks denote spinning sidebands. In case of the ^{7}Li NMR spectra the narrow NMR line at the highest temperature measured is compared with the non-narrowed line of the rigid lattice (dashed red line).

Discussion

The simulation of compressing a $BaLiF_3$ with a $SrLiF_3$ particle resulted in the formation of $Ba_{1-x}Sr_xLiF_3$ in agreement with experiment. The formation of very Sr-rich $Ba_{1-x}Sr_xLiF_3$ or even pure $SrLiF_3$, however, was not observed experimentally which indicates that these species might only be stable at high pressure. After the impact event, which might in fact lead to the formation of $SrLiF_3$, this compound would decompose again and later on react with residual $BaLiF_3$ until the reaction, forming $Ba_{1-x}Sr_xLiF_3$, is completed.

The simulation of the crystallization revealed the erroneous crystallization of Li ions at Ba/Sr sites and Ba/Sr at Li sites to be common. Although most of these defects are repaired since they seemingly impede further crystallization (see 'Methods' section), a few wrongly placed cations remained in the crystallized system, creating Ba/Sr-Li anti-site defects. Interestingly, these defects cannot be eliminated within the crystal, which means that their number should be independent of the temperature of the crystallized system, but depend on the synthesis parameters. Hence, the anti-site defect density of

$BaLiF_3$ might differ for different synthesis temperatures, -pressures etc.

The simulations revealed no ion motion in perfectly crystalline $BaLiF_3$, but only in defective $BaLiF_3$, notably close to Ba-Li anti-site defects as already proposed by Zahn et al.[25]. Furthermore, the replacement of a part of the Ba ions by Sr ions increased the ion mobility considerable, as shown by simulation and experiment, which is most likely caused by geometric frustration lowering the activation energies for ion migration.

Interestingly, the highest ion mobility was experimentally observed for the microcrystalline and single crystalline $BaLiF_3$ (figs. 6 and S8) which, however, showed a smaller ionic conductivity than the $BaLiF_3$ prepared by high-energy ball milling[26] (fig. S10). Also the ionic conductivity of the $Ba_{1-x}Sr_xLiF_3$ is not considerable increased compared to the one of the mechanosynthesized $BaLiF_3$[30] (fig. S10), despite its higher ionic mobility. Hence, it seems plausible to assume that the ion conductivity of nanocrystalline, mechanosynthesized $BaLiF_3$ and $Ba_{1-x}Sr_xLiF_3$ is governed by fast ion motion in the grain boundaries as was already assumed[26,27] and is in agreement with simulation (fig. S5).

However, the origin of the different ion mobilities in the different $BaLiF_3$ samples remains unclear. It should be noted that all $BaLiF_3$ samples investigated are phase pure and exhibit very similar lattice parameters[26,27]. The simulations indicate a higher defect density in the micro- and single crystalline material than in the mechanosynthesized $BaLiF_3$ since only the defective regions show ion mobility. This might be caused by a contamination introduced during the heat treatment. In fact, the $BaLiF_3$ single crystal shows an extrinsic part of ion conductivity indicating a contamination of the crystal[26] (fig. S10), despite the very careful synthesis procedure. The annealed microcrystalline sample, however, does not show any extrinsic conductivity in the temperature range measured[26], see fig. S10. Interestingly, the annealed $BaLiF_3$ shows a motional narrowing at lower temperature than the single crystal (fig. S8). Since the ionic conductivity of the single crystal is higher in this temperature regime, this indicates a larger number of mobile ions in single crystalline $BaLiF_3$ than in the annealed sample, supporting the assumption of some sort of contamination of the single crystal.

Another possible explanation could be a reduced anti-site defect density in mechanosynthesized $BaLiF_3$, since this kind of defect fosters ion mobility. In this regard it should be noted that vacancies seem to have no pronounced impact on ion mobility, indicating high activation energies for ion migration and, thus, also point defect formation. While a reduction of the number of mobile vacancies formed during crystallization would not be surprising in a nanocrystal, since they should soon end up at the surface of the crystallite, eliminating the vacancy, such mechanism would not work in case of anti-site defects. We therefore explore whether our simulations can disclose how ball milling could reduce the anti-site defect density.

Our simulations reveal defect repair mechanisms: ions condensing onto 'incorrect' lattice sites can subsequently move off the site to be replaced by the correct ion. However, this can only occur at a crystalline/amorphous interface and not deep within the crystal; the ball milling process could therefore facilitate the exposure of anti-site defects, deep within the crystal, to the surface. We now hypothesize as to how ball milling might facilitate this.

During milling, crystallites are repeatedly impacted and welded by the milling balls. We postulate that the repeated high-energy impacts, associated with ball milling, provides sufficient stress to initiate lattice slip - exposing defects, from 'deep' within the crystal, to a surface. Moreover, the impacts and the mechanical stress, induced by milling balls rolling over the crystallites, are also likely to cause localized abrasion and amorphisation of the crystallite surfaces[50] and regions near the surface allowing a localized recrystallization. Repair is now possible because anti-site defects can move off their (incorrect) lattice sites and be replaced by the correct ion from within the amorphous region. We also propose that lattice slip along grain boundaries (GB), induced by the mechanical stress associated with ball milling, might enable repair of the GB's[49]. In particular, previously

we predicted that uniaxial stress acting, upon a nanomaterial, can induce Ostwald ripening via a purging of the grain-boundaries to facilitate single nanocrystals from polycrystalline precursors[50]. Specifically, under high levels of stress - of the order of GPa - the material deformed plastically along the grain-boundary planes. We propose that ball milling can facilitate such high uniaxial stress and induce plastic deformation upon the sample to purge grain-boundaries from the material. We note that ball milling has been shown to induce pressures in the GPa-range[34]. The pressures occuring during ball milling employing the ball mill and milling conditions used in this study have been calculated to be around 0.4 GPa[51]. Moreover, the stresses associated with impacts between the balls and the sample are likely to be even higher.

We propose that the milling process might provide many localized anti-site defect repair attempts. Since point defects increase the brittleness of a material, it seems likely that defect rich regions are preferentially brought back to the surface.

We note that Prochowicz et al.[20] reported low defect levels in mechanochemically prepared perovskite-type $CH_3NH_3PbI_3$. Thus, a similar mechanism might have played a role in their synthesis.

Conclusions

We have simulated the crystallization of $Ba_{1-x}Sr_xLiF_3$ under conditions that mirror an impact event during mechanosynthesis using a high-energy ball mill. The simulations revealed that during crystallization, Ba-Li anti-site defects are formed, increasing the ionic mobility in their vicinity. Also the replacement of (a part of the) Ba ions by Sr ions increases the ion mobility considerably as shown by simulation and experiment. Both, experiment and simulation also revealed both ion species, F and Li, to be mobile in $BaLiF_3$. The lower ionic mobility in mechanosynthesized $BaLiF_3$ compared to thermally prepared $BaLiF_3$ was attributed to a lower defect density. This might be caused by contamination during the thermal treatments, or it could be facilitated by the mechanosynthesis technique, which repeatedly exposes anti-site defects to surfaces where they can be eliminated. If this assumption turns out to be correct, which remains to be tested in future work, it seems likely, that this process also occurs in other layered systems in which multiple ion species compete for sites during crystallization.

Acknowledgments

Financial support by the DFG, Germany, in the project DU 1668 1-1/1-2 is gratefully acknowledged. We are grateful to the UK Materials and Molecular Modelling Hub for computational resources, which are partially funded by EPSRC (EP/P020194/1). A. D. thanks A. Kuhn for fruitful discussions.

References

[1] Sorokin, N. I.; Sobolev, B. P. Nonstoichiometric Fluorides – Solid Electrolytes for Electrochemical Devices: A Review. Cryst. Rep. **2007**, 52, 842-863.

[2] Skinner, S. J.; Kilner, J. A. Oxygen ion conductors. Mater. Today **2003**, 6, 30-37.

[3] Chen, J.; Graetz, J. Study of Antisite Defects in Hydrothermally Prepared $LiFePO_4$ by in Situ X-ray Diffraction. ACS Appl. Mater. Interfaces **2011**, 3, 1380-1384.

[4] Paolella, A.; Bertoni, G.; Hovington, P.; Feng, Z.; Flacau, R.; Prato, M.; Colombo, M.; Marras, S.; Manna, L.; Turner, S.; van Tendeloo, G.; Guerfi, A.; Demopoulos, G.P.; Zaghib, K. Cation exchange mediated elimination of the Fe-antisites in the hydrothermal synthesis of $LiFePO_4$. Nano Energy **2015**, 16, 256-267.

[5] Gfroerer, T. H.; Zhang, Yong; Wanlass, W. M. An extended defect as a sensor for free carrier diffusion in a semiconductor. Appl. Phys. Lett. **2013**, 102, 012114.

[6] Lin, Y. ; Zhang, Y.; Liu, Z.; Su, L.; Zhang, J.; Wie, T.; Chen, Z. Interplay of point defects, extended defects, and carrier localization in the efficiency droop of InGaN quantum wells light-emitting diodes investigated using spatially resolved electroluminescence and photoluminescence. J. Appl. Phys. **2014**, 115, 023103.

[7] Yamada, Y.; Endo, M.; Wakamiya, A.; Kanemitsu, Y. Spontaneous Defect Annihilation in $CH_3NH_3PbI_3$ Thin Films at Room Temperature Revealed by Time-Resolved Photoluminescence Spectroscopy, J. Phys. Chem. Lett. **2015**, 6, 482-486.

[8] Bensalah, A.; Shimamura, K.; Fujita, T.; Sato, H.; Nikl, M. and Fukuda, T. Growth and characterization of $BaLiF_3$ single crystal as a new optical material in the VUV region. J. Alloys Compd. **2003**, 348, 258-262.

[9] Coutts, D. W.; McGonigle, A. J. S. Cerium-Doped Fluoride Lasers. IEEE J. Quant. Electron. **2004**, 40, 1430-1440.

[10] Jiang, D.; Wang, W.; Zhang, L.; Zheng, Y.; Wang, Z. Insights into the Surface-Defect Dependence of Photoreactivity over CeO_2 Nanocrystals with Well-Defined Crystal Facets. ACS Catal. **2015**, 5, 4851-4858.

[11] Trovarelli, A.; Llorca, J. Ceria Catalysts at Nanoscale: How Do Crystal Shapes Shape Catalysis? ACS Catal. **2017**, 7, 4716-4735.

[12] Suresh, S.; Li, J. Materials Science: Deformation of the ultra-strong. Nature **2008**, 456, 716-717.

[13] Kim, C. H. ; Qi, G.; Dahlberg, K.; Li, W. Strontium-Doped Perovskites Rival Platinum Catalysts for Treating NO_x in Simulated Diesel Exhaust. Science **2010**, 327, 1624-1627.

[14] Zhang, B.; Chen, G.; Li, H. Review of perovskite structure solid state lithium ion conductor. J. Rare Earths **2006**, 24, 132-138.

[15] de Souza, E. C. C.; Muccillo, R. Properties and Applications of Perovskite Proton Conductors. Mat. Res. **2010**, 13, 385-394.

[16] Stølen, S.; Bakken, E.; Mohn, C. E. Oxygen-deficient perovskites: linking structure, energetic and ion transport. Phys. Chem. Chem. Phys. **2006**, 8, 429-447.

[17] Zeb, A.; Milne, S. J. High temperature dielectric ceramics: a review of temperature-stable high-permittivity perovskites. J. Mater. Sci. Mater. El. **2015**, 26, 9243-9255.

[18] Chauhan, A.; Patel, S.; Vaish, R.; Bowen, C. R. Anti-Ferroelectric Ceramics for High Energy Density Capacitors. Materials **2015**, 8, 8009-8031.

[19] Uchino, K. Glory of piezoelectric perovskites. Sci. Technol. Adv. Mater. **2015**, 16, 046001.

[20] Prochowicz, D.; Franckevicious, M.; Cieślak, A. M.; Zakeeruddin, S. M.; Grätzel, M. and Lewiński, J. Mechanosynthesis of the hybrid perovskite $CH_3NH_3PbI_3$: characterization and the corresponding solar cell efficiency. J. Mater. Chem. A **2015**, 3, 20772-20777.

[21] Boumriche, A.; Gesland, J. Y.; Bulou, A.; Rousseau, M.; Fourquet, J. L.; Hennion, B. Structure and dynamics of the inverted perovskite $BaLiF_3$. Solid State Commun. **1994**, 91, 125-128.

[22] Yalcin, B. G.; Salmankurt, B.; Duman, S. Investigation of structural, mechanical, electronic, optical, and dynamical properties of cubic $BaLiF_3$, $BaLiH_3$, and $SrLiH_3$. Mater. Res. Express **2016**, 3, 036301.

[23] Dubinskii, M. A.; Schepler, K. L.; Semashko, V. V.; Yu Abdulsabirov, R.; Galjautdinov, B. M.; Korableva, S. L.; Naumov, A. K. Ce^{3+}:$LiBaF_3$ as New Prospective Active Material for Tunable UV Laser with Direct UV Pumping. OSA TOPS **1997**, 10, 30-34.

[24] Jackson, R. A.; Valerio, M. E. G.; de Lima, J. F.; Computer modelling of $BaLiF_3$: I. Interionic potentials and intrinsic defects. J. Phys.: Condens. Matter **1996**, 8, 10931-10937.

[25] Zahn, D.; Herrmann, S.; Heitjans, P. On the mechanisms of ionic conductivity in $BaLiF_3$: a molecular dynamics study. Phys. Chem. Chem. Phys. **2011**, 13, 21492-21495.

[26] Düvel, A.; Wilkening, M.; Uecker, R.; Wegner, S.; Šepelák, V.; Heitjans, P. Mechanosynthesized nanocrystalline $BaLiF_3$: The impact of grain boundaries and structural disorder on ionic transport. Phys. Chem. Chem. Phys. **2010**, 12, 11251-11262.

[27] Düvel, A.; Wilkening, M.; Wegner, S.; Feldhoff, A.; Šepelák, V.; Heitjans, P. Ion conduction and dynamics in mechanosynthesized nanocrystalline $BaLiF_3$. Solid State Ionics **2011**, 184, 65-69.

[28] Šepelák, V.; Düvel, A.; Wilkening, M.; Becker K.-D. and Heitjans, P. Mechanochemical reactions and syntheses of oxides. Chem. Soc. Rev. **2013**, 18, 7507-7520.

[29] James, S. L.; Adams, C. J.; Bolm, C.; Braga, D.; Collier, P.; Friščić, T.; Grepioni, F.; Harris, K. D. M.; Hyett, G.; Jones, W.; Krebs, A.; Mack, J.; Maini, L.; Orpen, A. G.; Parkin, I. P.; Shearouse, W. C.; Steed, J. W.; Waddell, D. C. Mechanochemistry: opportunities for new and cleaner synthesis. Chem. Soc. Rev. **2012**, 41, 413-447.

[30] Düvel, A.; Wegner, S.; Efimov, K.; Feldhoff, A.; Heitjans, P.; Wilkening, M. Access to metastable complex ion conductors via mechanosynthesis: preparation, microstructure and conductivity of (Ba,Sr)LiF_3 with inverse perovskite structure. J. Mater. Chem. **2011**, 21, 6238.
[31] Düvel, A.; Romanova, E.; Sharifi, M.; Freude, D.; Wark, M.; Heitjans, P.; Wilkening, M. Mechanically Induced Phase Transformation of γ-Al_2O_3 into α-Al_2O_3. Access to Structurally Disordered γ-Al_2O_3 with a Controllable Amount of Pentacoordinated Al Sites. J. Phys. Chem. C **2011**, 115, 22770-22780.
[32] Düvel, A.; Ruprecht, B.; Heitjans, P.; Wilkening, M. Mixed Alkaline-Earth Effect in the Metastable Anion Conductor $Ba_{1-x}Ca_xF_2$ ($0 \le x \le 1$): Correlating Long-Range Ion Transport with Local Structures Revealed by ultrafast ^{19}F MAS NMR. J. Phys. Chem. C **2011**, 115, 23784-23789.
[33] Düvel, A.; Bednarcik, J.; Šepelák, V.; Heitjans, P.; Mechanosynthesis of the Fast Fluoride Ion Conductor $Ba_{1-x}La_xF_{2+x}$: From the Fluorite to the Tysonite Structure. J. Phys. Chem. C **2014**, 118, 7117-7129.
[34] Hashishin, T.; Tan, Z.; Yamamoto, K.; Qiu, N.; Kim, J.; Numako, C.; Naka, T.; Valmalette J. C. and Ohara, A. Quenching ilmenite with a high-temperature and high pressure phase using super-high-energy ball milling. Sci. Rep. **2014**, 4, 4700.
[35] Boumriche, A.; Gesland, J. Y.; Bulou, A.; Rousseau, M.; Fourquet, J. L.; Hennion, B. Structure and dynamics of the inverted perovskite $BaLiF_3$. Solid State Commun. **1994**, 91, 125-128.
[36] Sayle, T. X. T.; Parker, S. C. and Sayle, D. C. Shape of CeO_2 nanoparticles using simulated amorphisation and recrystallization. Chem. Commun. **2004**, 2438-2439.
[37] Sayle, D. C. and Sayle, T. X. T. High-Pressure Crystallisation of TiO_2 Nanoparticles. J. Comput. Theor. Nanos. **2007**, 4, 299-308.
[38] Khenata, R.; Daoudi, B.; Sahnoun, M.: Baltache, H.; Rérat, M.; Reshak, A. H.; Bouhafs, B.; Abid, H.; Driz, M. Structural, electronic and optical properties of fluorite-type compounds. Eur. Phys. J. B **2005**, 47, 63-70.
[39] Wintersgill, M.; Fontanella, J.; Andeen, C.; Schuele, D. The temperature variation of the dielectric constant of "pure" CaF_2, SrF_2, BaF_2 and MgO. J. Appl. Phys. **1979**, 50, 8259-8261.
[40] Gale, J. D. GULP: Capabilities and prospects. Z. Krist. **2005**, 220, 552-554.
[41] Todorov, I. T.; Smith, W.; Trachenko, K.; Dove, M. T.; DL_Poly_3: new dimensions in molecular dynamics simulations via massive parallelism. J. Mater. Chem. **2006**, 16, 1911-1918.
[42] Chandran, C. V.; Hempel, G.; Braeuniger, T. ^{19}F-decoupling of half-integer spin quadrupolar nuclei in solid-state NMR: Application of frequency-swept decoupling methods, Solid State Nucl. Magn. Reson. **2010**, 40, 84-87.
[43] Fukushima, E.; Roeder, S. B. W. Experimental Pulse NMR. Addison-Wesley: Reading, MA, 1981.
[44] Chadwick, A. V.; Davis, S. R.; de Lima, J. F.; Valerio, M. E. G.; Baldochi, S. L. An EXAFS study of the Ni dopant site in $BaLiF_3$. J. Phys.: Condens. Matter **1996**, 8, 10679-10685.
[45] Valerio, M. E. G.; Jackson, R. A.; de Lima, J. F. Computer modeling of $BaLiF_3$: Defects produced by divalent dopants. J. Phys.: Condens. Matter **1998**, 10, 3353-3358.
[46] Yalcin, B. G.; Salmankurt, B.; Duman, S. Investigation of structural, mechanical, electronic, optical, and dynamical properties of cubic $BaLiF_3$, $BaLiH_3$, and $SrLiH_3$. Mater. Res. Express **2016**, 3, 036301.
[47] Düvel, A.; Heitjans, P.; Fedorov, P.; Scholz, G.; Cibin, G.; Chadwick, A. V.; Pickup, D. M.; Ramos, S.; Sayle, L. W. L.; Sayle, E. K. L.; Sayle, T. X. T.; Sayle, D.C. Is Geometric Frustration Induced Disorder a Recipe for High Ionic Conductivity? J. Am. Chem. Soc. **2017**, 139, 5842-5848.
[48] Kaliaperumal, R.; Sears, R. E. J.; Finch, C. B. ^{19}F shielding anisotropy in $RbCaF_3$. J. Chem. Phys. **1987**, 87, 68-72.
[49] Yamane, Y.; Yamada, K.; Inoue, K.; Mechanochemical synthesis and order-disorder phase transition in fluoride ion conductor $RbPbF_3$. Solid State Ionics **2008**, 179, 605-610.
[50] Caddeo, F.; Corrias, A.; Sayle, D.C. Tuning the Properties of Nanoceria by Applying Force: Stress-Induced Ostwald Ripening. J. Phys. Chem. C **2016**, 120, 14337-14344.
[51] Düvel, A. NMR- und impedanzspektroskopische Untersuchungen zur Dynamik und lokalen Struktur in

mechanochemisch dargestellten Nichtgleichgewichtsphasen. Doctoral Dissertation. Leibniz University Hannover, 2014, page 37.

Supporting information

The Supporting Information is available free of charge on the ACS Publications website.

Interatomic potential parameters, further molecular graphics, further ^{19}F and ^{7}Li MAS NMR spectra, static ^{7}Li NMR spectra, Arrhenius plot of the dc conductivities.
Videos showing the crystallization and the F ion mobility near an anti-site defect.

For Table of Contents Use Only

Formation and elimination of anti-site defects during crystallization in perovskite $Ba_{1-x}Sr_xLiF_3$

A. Düvel, L. M. Morgan, C. Vinod Chandran, P. Heitjans, D.C. Sayle

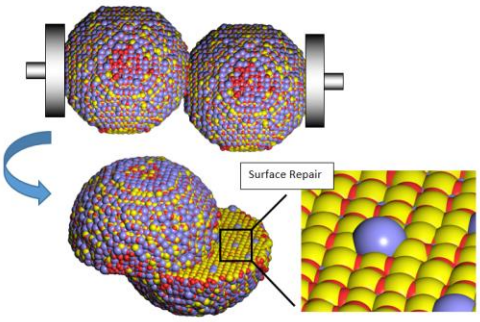

Synopsis

MD Simulation of the crystallization of $Ba_{1-x}Sr_xLiF_3$ showed the formation of Ba-Li anti-site defects, which increase the mobility of F and Li ions in their vicinity. Synthesis of $BaLiF_3$ by ball milling seems to decrease the density of this defect-type compared to thermally prepared $BaLiF_3$ presumably by exposing the defects to the crystallite surface where they can be repaired.